JOURNAL OF THERMOPHYSICS AND HEAT TRANSFER
Vol. 23, No. 2, April–June 2009

Oxidation of ZrB_2–SiC Ultrahigh-Temperature Ceramic Composites in Dissociated Air

Jochen Marschall* and Dušan A. Pejaković†
SRI International, Menlo Park, California 94025
William G. Fahrenholtz,‡ Greg E. Hilmas,§ and Sumin Zhu¶
Missouri University of Science and Technology, Rolla, Missouri 65409
Jerry Ridge**
NASA Ames Research Center, Moffett Field, California 94035
and
Douglas G. Fletcher,†† Cem O. Asma,‡‡ and Jan Thömel§§
von Kármán Institute for Fluid Dynamics, 1640 Rhode-Saint-Genèse, Belgium

DOI: 10.2514/1.39970

The oxidation behavior and surface properties of hot-pressed ZrB_2–SiC ultrahigh-temperature ceramic composites are investigated under aerothermal heating conditions in the high-temperature, low-pressure partially dissociated airstream of the 1.2 MW Plasmatron facility at the von Kármán Institute for Fluid Dynamics. Samples are oxidized at different flow enthalpies for exposure times of up to 20 min at surface temperatures ranging from 1250 to 1575°C. The microstructure and composition of the resulting oxide layers are characterized using electron and optical microscopies, x-ray diffraction, and energy-dispersive x-ray analysis. Comparisons are made with samples oxidized under similar temperature and pressure conditions in a furnace test environment in which atomic oxygen concentrations are negligible. Changes in surface optical properties are documented using spectral reflectance measurements, and effective catalytic efficiencies are estimated using computational fluid dynamics calculations together with measured surface temperatures and heat fluxes.

Nomenclature

H	=	enthalpy, $J \cdot kg^{-1} \cdot K^{-1}$
$\dot{m}$	=	mass flow rate, $kg \cdot s^{-1}$
P	=	pressure, Pa
q	=	heat flux, $W \cdot m^{-2}$
R_m	=	model radius, m
T	=	temperature, K
u_1, u_2	=	dimensionless velocity gradients in the x and y directions
u, v	=	velocity in the x and y directions, $m \cdot s^{-1}$
V	=	dimensionless velocity in the y direction
x, y	=	surface parallel and normal coordinate axes
γ	=	atomic recombination coefficient
γ'	=	catalytic efficiency
Δ	=	nondimensional boundary-layer thickness
δ	=	boundary-layer thickness, m
ε	=	emittance
σ	=	Stefan–Boltzmann constant; 5.67×10^{-8} $W \cdot m^{-2} \cdot K^{-4}$

Subscripts

cond	=	conduction
cw	=	cold wall
dyn	=	dynamic
e	=	boundary-layer edge
stat	=	static
w	=	wall

Received 23 July 2008; revision received 16 January 2009; accepted for publication 18 January 2009.

*Senior Research Scientist, Molecular Physics Laboratory, 333 Ravenswood Avenue; jochen.marschall@sri.com. Senior Member AIAA.

†Research Physicist, Molecular Physics Laboratory, 333 Ravenswood Avenue. Member AIAA.

‡Professor, Department of Materials Science and Engineering, 223 McNutt Hall; billf@mst.edu.

§Professor, Department of Materials Science and Engineering, 223 McNutt Hall; ghilmas@mst.edu.

¶Ph.D. Candidate, Department of Materials Science and Engineering, 223 McNutt Hall; Sumin.Zhu@us.vesuvius.com.

**Research Engineer, Thermal Protection Materials and Systems Branch, Building 234; also, ELORET Corporation, Sunnyvale, California 94086; jerome.w.ridge@nasa.gov.

††Past Head, Aeronautics and Aerospace Department; currently, Professor, Mechanical Engineering, University of Vermont, 201 Votey Hall, 33 Colchester Avenue, Burlington, VT, 05405; douglas.fletcher@uvm.edu. Associate Fellow AIAA.

‡‡Research Engineer. Aeronautics and Aerospace Department, Ch. De Waterloo 72; asma@vki.ac.be.

§§Ph.D. Candidate, Aeronautics and Aerospace Department. Ch. De Waterloo 72; jan.thoemel@vki.ac.be. Student Member AIAA.

I. Introduction

ULTRAHIGH-TEMPERATURE ceramic (UHTC) composites containing transition metal borides, carbides, and nitrides are under intensive investigation for applications in extreme environments [1,2]. UHTC composites based on ZrB_2 and HfB_2, in combination with silica formers such as SiC and $MoSi_2$, are particularly attractive for high-temperature aerospace applications, such as leading-edge and control surface components on hypersonic vehicles. Both ZrB_2 and HfB_2 and their transition metal oxides, ZrO_2 and HfO_2, have extremely high melting points (>2500°C). Hafnium and zirconium diborides have higher thermal conductivities compared with their carbide and nitride analogs, giving them a performance advantage for sharp leading-edge components for which drawing heat away from the stagnation point region is essential. Composites based on ZrB_2 have the additional benefits of lower density and lower cost compared with HfB_2-based composites.

The oxidation behavior of ZrB_2 and its composites has been studied by many researchers using thermal gravimetric analysis

(TGA) or conventional furnace environments [3–14]. During isothermal oxidation at temperatures between 1200 and 1600°C and pressures near 1 atm, an oxide scale consisting of two distinct layers develops on the surface of ZrB_2–SiC composites [4,12]. The outer layer is a dense oxide scale consisting of a silica-rich glass with some embedded ZrO_2 crystallites. This glassy scale is separated from the underlying virgin material by a partially oxidized and somewhat porous interlayer, containing ZrO_2 and/or ZrB_2, from which the SiC has been partially or fully depleted by active oxidation.

Virgin ZrB_2–SiC surfaces oxidize initially through the parallel net reactions $ZrB_2 + 5/2O_2 \rightarrow ZrO_2 + B_2O_3(l)$ and $SiC + 3/2O_2 \rightarrow SiO_2 + CO(g)$. Liquid B_2O_3 mixes with amorphous SiO_2 to form a borosilicate glass that seals the surface. However, B_2O_3 has a high vapor pressure that causes it to evaporate preferentially from the glassy phase and leave behind a silica-rich material. As the silica-rich-layer thickens, it limits the inward diffusion of oxygen to the virgin material below, slowing oxidation and lowering the oxygen partial pressure in the reaction zone [12]. At sufficiently low oxygen pressures, the oxidation of ZrB_2 becomes negligible and the oxidation of silicon carbide becomes "active," proceeding by the reaction $SiC + O_2 \rightarrow SiO(g)$ and $CO(g)$ [12,15].

Oxidation rates are commonly quantified by measuring the thickness of the oxide layers or by measuring the mass change of the specimen. For oxidation of ZrB_2–SiC, these rates are normally proportional to the square root of time (i.e., parabolic kinetics) consistent with diffusion-limited oxidation. Oxidation under lower total pressures and higher temperatures can result in evaporation of the SiO_2 in addition to the B_2O_3, leaving behind a single outer layer of porous ZrO_2 and resulting in rapid, linear oxidation kinetics [13].

In both conventional TGA and furnace experiments, the gas environment is in thermal equilibrium with the test specimen. The thermochemical makeup of the test gas is determined by the feed gas composition and test temperature and pressure through equilibrium chemistry. In contrast, in hypersonic flight environments, large temperature gradients exist between the leading-edge surfaces and the boundary layer and shock layer edges. The gas temperature in a shock layer can easily exceed 10,000°C, resulting in an energetic gas mixture whose thermochemical makeup may contain ions, atoms, and molecules in highly energetic states. The shocked gas will undergo thermochemical relaxation as it nears the colder surface, but typically will not reach chemical equilibrium at the temperature of the surface. One ramification of this thermochemical nonequilibrium is that UHTC materials on leading-edge surfaces may interact with significant concentrations of highly reactive atomic oxygen.

In this paper, we report the results of oxidation tests performed in high-temperature, low-pressure dissociated airflows on hot-pressed ZrB_2 composites containing 30 vol% SiC (ZrB_2–30SiC). The ZrB_2–30SiC specimens were manufactured at the Missouri University of Science and Technology (Missouri S&T) in Rolla, Missouri, and tested in the 1.2 MW Plasmatron facility of the von Kármán Institute for Fluid Dynamics (VKI) in Rhode-Saint-Genèse, Belgium. The microstructure and composition of the resulting oxide layers are characterized and compared with oxidation studies performed at SRI International in a furnace under similar temperature and total pressure conditions. Results are discussed in terms of thermodynamic considerations, as well as previously published oxidation studies in furnace and arcjet environments. Changes in optical properties resulting from surface oxidation are characterized by spectral reflectance measurements. The effective catalytic efficiencies for oxygen- and nitrogen-atom recombination on the oxidizing surfaces are estimated using computational fluid dynamics (CFD) simulations in conjunction with measured surface temperatures and heat fluxes.

II. Materials

UHTC specimens were prepared from commercial powders supplied by H.C. Starck (grade B ZrB_2 and UF-10 SiC). Powders were attrition milled using tungsten carbide media for 2 h in hexane and then dried by rotary evaporation. The dried powders were put into graphite dies that were lined with boron-nitride-coated graphite foil. Densification was accomplished by hot pressing (Thermal Technology FP-20-3560). The hot press was heated under rough vacuum (~20 Pa) at $\sim 20°C \cdot min^{-1}$ to 1450°C, held for 1 h, then heated at the same rate to 1650°C and held for another hour. The hot press was then backfilled to 1 atm with argon and heated at $\sim 20°C\ min^{-1}$ to a temperature of 1900°C, at which a uniaxial pressure of 32 MPa was applied and the specimens were held for 45 min. At the end of this hold time, the hot press was cooled at $\sim 20°C \cdot min^{-1}$ to room temperature and, at ~1750°C, the load was removed.

After removal from the dies, the hot-pressed samples were approximately 3–4 mm thick with diameters of about 32 mm. The large faces of the disks were diamond ground flat and parallel at Missouri S&T and then shipped to Bomas Machine Specialties, Inc. (Sommerville, Massachusetts), where a 30 deg bevel was diamond ground into the disk edge, leaving a small face with a diameter of 26.6 mm, as shown in Fig. 1a. This bevel was used to hold the samples in the standard ESA 50 mm stagnation point test fixture used in VKI's Plasmatron facility; see Fig. 1b.

Machined UHTC specimens were cleaned with acetone in an ultrasonic bath, rinsed with distilled water, and dried in a 100°C oven. The mass and thickness of each specimen were measured before testing. Specimen densities calculated from these measurements and the known sample geometry ranged from 5.22 to $5.36\ g \cdot cm^{-3}$. The theoretical density of ZrB_2–30SiC, assuming densities of $6.09\ g \cdot cm^{-3}$ for ZrB_2 and $3.21\ g \cdot cm^{-3}$ for SiC, is $5.23\ g \cdot cm^{-3}$. The slightly higher specimen densities were due to the presence of a small volume fraction of tungsten carbide contamination from the milling media [16].

III. Experiment

A. Plasmatron Facility

Plasma oxidation experiments were performed in the 1.2 MW Plasmatron Facility at VKI [17,18]. This facility uses a high-frequency, high-power, high-voltage (400 kHz, 1.2 MW, 2 kV) solid-state power supply to generate a high-enthalpy gas flow by inductive coupling in a 160-mm-diam plasma torch. The plasma flow was directed into a 2.5-m-long, 1.4-m-diam vacuum chamber equipped with multiple portholes and windows for optical diagnostics. Test models and probes for measuring dynamic pressure

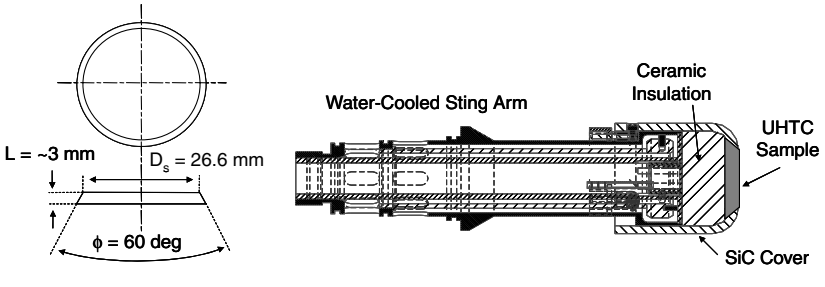

Fig. 1 Geometry: a) UHTC test specimens, and b) stagnation point specimen holder.

and stagnation point heating rates were mounted on water-cooled arms that could be swung into and out of the flow on demand.

The cold-wall stagnation point heat flux, q_{cw}, was measured during each experimental run using a water-cooled copper calorimeter installed flush with the surface along the centerline of the water-cooled copper probe. Heat flux values were determined from the temperature change and mass flow rate of the water used to cool the calorimeter. The size and external shape of the probe was identical to the specimen holder so that important flow parameters (dynamic pressure, velocity gradient) were reproduced. Both the probe and calorimeter had polished copper surfaces that were assumed to be fully catalytic to N- and O-atom surface recombination.

Sample surface temperatures were measured by a two-color pyrometer (Marathon Series MR1SC, Raytek Corporation, Santa Cruz, California) at an acquisition rate of 1 Hz. The pyrometer uses two overlapping infrared wavelength bands at 0.8–1.1 and 1.0–1.1 μm to measure temperatures from 1000 to 3000°C. Thermal emission from the sample was collected through a glass window at an incident angle of 29 deg off normal. The pyrometer was previously calibrated with the same window in place using a blackbody radiation source; temperature measurements are believed to be accurate to ± 10°C.

Unlike arcjet wind tunnels, which operate in the supersonic flow regime, inductively coupled plasma (ICP) facilities like the Plasmatron at VKI are typically operated in the subsonic flow regime. For materials-science-oriented studies, this operating regime has the advantage that the conditions in the plasma stream are much more likely to be at or near thermal and chemical equilibrium, making estimates of the gas chemical composition at the specimen surface more robust. In addition, metal contaminates that are often present in arcjet flows because of the electrode sputtering are absent in ICP facilities because the plasma flows see no metal surfaces inside the torch head.

B. Plasmatron Test Conditions

The critical environmental parameters driving UHTC oxidation are the sample temperature, the gas pressure, and the chemical composition of the gas interacting with the sample surface. These parameters are essential for correlating the extent of UHTC oxidation with different test environments and understanding the kinetic aspects of oxide scale formation. Whereas surface temperature and gas pressure can be measured directly, the gas composition at the specimen surface cannot. Computational fluid dynamics simulations of the plasma freestream and the boundary layer around the model holder are used to compute the gas composition from known Plasmatron operating parameters and available surface temperature, pressure, and heat flux measurements made on the sample and probe during each test run. This is a two-step process. First, the freestream plasma flow conditions at the boundary-layer edge along the stagnation point centerline are rebuilt for each Plasmatron operating condition, using measured quantities and known facility and geometric parameters; then, these boundary-layer-edge conditions are used together with the measured sample surface temperature to compute the gas composition and temperature through the boundary layer to the sample surface. This procedure also couples the measured surface temperature to the boundary-layer-edge conditions through an energy balance at the sample surface, providing an estimation of the catalytic efficiency of the oxidizing surface for O- and N-atom recombination.

The CFD codes used for this procedure were developed at VKI and include the VKI boundary-layer code [19,20] and the VKI ICP code [21,22], both of which use the PÉGASE library to perform thermodynamic and transport property calculations [23]. The performance and validation of these codes and examples of their use in simulating flows in the Plasmatron can be found in the referenced papers. The ICP code simulates the flow inside the plasma torch and around the test sample in the vacuum chamber by solving the time-averaged magnetohydrodynamic equation at low Mach and low magnetic Reynolds numbers, assuming axisymmetric flow and local thermodynamic equilibrium. The boundary-layer code solves the boundary-layer equations for an axisymmetric or two-dimensional steady laminar flow of chemically reacting gas over a catalytic surface, including thermal and chemical nonequilibrium. The code provides computations of the stagnation point heat flux with a functional dependence:

$$q_w = q_w(\gamma', T_w, P_e, T_e, \Delta, u_1, u_2, V_e) \tag{1}$$

where γ' is the catalytic recombination efficiency, T_w is the wall temperature, T_e and P_e are the gas temperature and pressure at the boundary-layer edge, Δ is the nondimensional boundary-layer thickness, V_e is the nondimensional axial velocity, u_1 is the nondimensional radial velocity gradient, and u_2 is the nondimensional axial derivative of the radial velocity gradient.

Figure 2 illustrates the relationship of the stagnation point boundary-layer region to the various parameters given earlier; u and v are the velocities along the x and y axes, and R_m is the radius of the axisymmetric test model.

Together, these two codes were used to rebuild the flow conditions at the boundary-layer edge from the cold-wall heat flux and dynamic pressure measurements. The four nondimensional boundary-layer parameters were computed by the ICP code for each Plasmatron test condition, given the test and Plasmatron geometries, the power coupled into the gas, the gas mass flow, and the static pressure. With the assumption that the local thermodynamic equilibrium holds at the boundary-layer edge, these computed nondimensional parameters served as inputs to the boundary-layer code. By taking the measured cold-wall heat flux as fully catalytic ($T_w = 300$ K, $\gamma' = 1$), values of T_e and V_e could be iteratively adjusted until the computed and measured heat fluxes agreed. The final temperature, T_e, determined the enthalpy of the gas at the boundary-layer edge, H_e.

Once the boundary-layer edge conditions for a particular test condition were determined, the VKI boundary-layer code could compute a heat flux abacus, $q_w = q_w(\gamma', T_w)$, where all other variables in Eq. (1) were fixed. The catalytic efficiency of a test specimen exposed to the same plasma flow was estimated by locating measured specimen surface temperature and hot-wall heat flux values on this abacus [24]. For each point on the abacus, the VKI boundary-layer code concurrently computed the concentrations of O, O_2, N, N_2, and NO species in the gas phase above the specimen surface. Thus, the location of each test on the heat flux abacus also determined the particular CFD solution used to estimate the gas composition at the sample surface.

Note that the catalytic recombination efficiency γ' used in the VKI boundary-layer code is the product of the species recombination coefficient, γ (the fraction of species–wall collisions that results in recombination), and the energy accommodation coefficient, β (the fraction of exothermic recombination energy transferred to the wall). The distinction between these two recombination efficiencies has been discussed by Bedra and Balat-Pichelin [25]; the two efficiencies are only equivalent in the case of ideal energy accommodation, $\beta = 1$. The VKI boundary-layer code also assumes that the catalytic efficiency is the same for O and N atoms ($\gamma'_O = \gamma'_N$) and does not include NO as a heterogeneous reaction product.

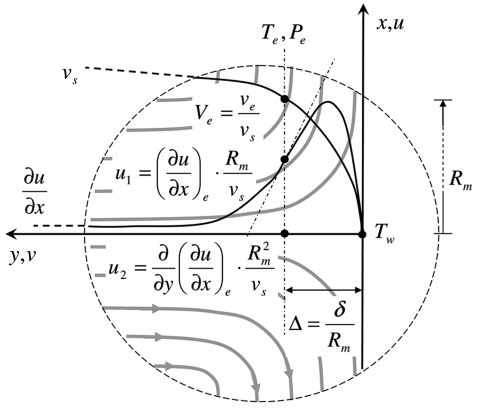

Fig. 2 General schematic diagram of the stagnation point boundary-layer region.

C. Furnace Oxidations

Furnace oxidations were performed in a tube furnace with resistive molybdenum disilicide heating elements capable of operating at 1600°C in air (Model 1610-20, CM Furnaces, Bloomfield, New Jersey). Samples were place on top of a "D-shaped" alumina substrate and positioned at the furnace midpoint inside a 45-mm-diam high-purity alumina tube. The furnace tube was sealed with vacuum-tight, water-cooled compression fittings at both ends. Air (Matheson Ultra Zero Grade, 99.999%) and argon (Matheson Ultra High Purity Grade, 99.999%) were introduced at one end through electronic mass flow controllers at a rate of 1 l/ min and evacuated at the opposite end by a high-capacity roots blower pumping system. Gas pressures were measured using a 100 torr capacitance manometer and maintained at the desired 10^4 Pa (75 torr) pressure level by adjusting a throttling valve inline with the vacuum system.

Samples were heated to either 1250 or 1575°C at a rate of approximately $10°C \cdot min^{-1}$ under a flow of pure argon. At the target temperature, the flow was switched from argon to air for the desired oxidation time. After the oxidation was completed, the gas flow was switched back to argon as the sample was cooled at a similar rate. The UHTC samples exposed to representative heating cycles of 1250 or 1575°C under pure argon flows showed no surface oxidation, confirming that oxygen impurities in argon and air leaks into the vacuum system were insignificant.

D. Sample Characterization

Sample masses and thicknesses were measured before and after testing using a Mettler Toledo XP105 analytical balance with 0.01 mg resolution and a Mitutoyo Model 543-272 Digimatic Indicator with 0.01 mm resolution. Sample thickness was measured at five locations, at the center and at four symmetric locations on a concentric 1.0-cm-diam circle, and averaged.

The room-temperature, hemispherical-directional spectral reflectance of several pre- and posttest UHTC samples was measured using two spectrophotometers fit with integrating spheres. A PerkinElmer Lambda 9 spectrophotometer (0.25–2.5 μm) was used to span the near ultraviolet to near infrared range and a BIORAD FTS-40 spectrophotometer (2.5–18.0 μm) was used for longer infrared wavelengths.

Posttest samples were prepared for microscopy by cutting specimens perpendicular to their oxidized faces and polishing the cross sections to a 0.25 μm finish using diamond abrasives. Microstructure and composition analyses were performed by field emission scanning electron microscopy (SEM, Model S4700, Hitachi, Japan) along with energy-dispersive x-ray spectroscopy (EDS, Model Phoenix, EDAX, Inc., Mahwah, New Jersey). Grazing incidence x-ray diffraction (GXRD; X'Pert MRD, Panalytical, Almelo, The Netherlands) with Ni-filtered Cu Kα radiation was used to determine the crystalline phases present in the oxidized surface layers. The grazing angle for GXRD was set to 1 deg, which resulted in a penetration depth of less than ~200 nm into the specimen. To examine the partially SiC-depleted interlayer with this technique, the silica-rich outer layer was removed by polishing parallel to the original surface. An optical microscope was used to verify material removal so that the partially SiC-depleted interlayer was fully exposed. X-ray photoelectron spectroscopy (XPS; AXIS 165, Cratos Analytical, Kyoto, Japan) was used to acquire the nitrogen bonding information on the posttest surface layer of one sample (sample 9).

IV. Experimental Results

A. Measured and Derived Test Conditions

All UHTC tests reported here were performed with an air mass flow rate, $\dot{m}$, of $16\ g \cdot s^{-1}$ and a static chamber pressure, P_{stat}, of 10^4 Pa. Freestream enthalpy was varied by adjusting the Plasmatron power between 150 and 210 kW, resulting in measured dynamic pressures ranging from 24 to 39 Pa and cold-wall heat fluxes ranging from 51 to 123 $W \cdot cm^{-2}$. The Plasmatron operating conditions and derived boundary-layer-edge conditions for each test are listed in Table 1.

Preliminary tests showed that inserting and removing the UHTC specimens rapidly from the plasma stream under these conditions caused the SiC covers on the model holders to fracture due to thermal shock. Therefore, specimens were moved into the plasma flows at low power (~100 kW) and the power was increased slowly to its target value. Similarly, after a desired exposure time, the power was decreased slowly to ~100 kW until the surface temperature dropped below 1100°C, before shutting the power off. Both the power ramp-up and ramp-down times were on the order of 1 min.

Target test times were measured from the moment the sample was inserted into the flow until to the moment that the power was ramped down. The test times at quasi-steady surface temperatures were shorter and were estimated from the transient temperature profiles. A typical transient temperature profile is given in Fig. 3 for sample 9, tested at 210 kW for a target time of 10 min.

The heating conditions for the entire UHTC test series are listed in Table 2. The second column of Table 2 gives both the target test time and (in brackets) the estimated time at a quasi-steady surface temperature. Quasi-steady surface temperatures typically exhibited fluctuations of tens of degrees Celsius (as seen in Fig. 3) and are reported to the nearest 10 deg in column 3 of Table 2. The hot-wall heat fluxes at the UHTC surfaces listed in Table 2 are not measured directly, but estimated from a radiative equilibrium calculation as $q_w = \varepsilon\sigma T_w^4 + q_{cond}$, with $\varepsilon = 0.75$ or 0.90, and $q_{cond} = 0$. The simplification $q_{cond} = 0$ causes a slight underestimation of the true hot-wall heat flux; however, this underestimation is small compared with errors introduced by uncertainty in the sample emittance.

The emittance values $\varepsilon = 0.75$ and 0.90 are reasonable for oxidizing ZrB_2–SiC surfaces, and each value is supported by some indirect experimental evidence as will be discussed in Sec. IV.C. The hot-wall heat flux estimated for $\varepsilon = 0.75$ is 17% smaller than for $\varepsilon = 0.90$, locating the tests at slightly different points (T_w, q_w) on the heat flux abacus computed using the VKI boundary-layer code. This, in turn, leads to slightly different values of derived recombination coefficients and species concentrations at the specimen surface.

Tables 3 and 4 list the values of γ'; the number densities of N_2, N, and O; and the number density ratios of O/O_2 and O/NO for $\varepsilon = 0.75$ and 0.90, respectively. The derived catalytic efficiencies are about 3–7 times larger for $\varepsilon = 0.90$ than for 0.75, because a greater chemical

Table 1 Plasmatron operating conditions, where $P_{stat} = 10^4$ Pa and $\dot{m} = 16\ g \cdot s^{-1}$ for all tests

Test-Sample	Power, kW	q_{cw}, $W \cdot cm^{-2}$	P_{dyn}, Pa	H_e, $kJ \cdot g^{-1}$	T_e, °C	v_e, ms^{-1}
5-20	150	51.0	24	11.2	4567	87.5
6-16	160	71.5	25	15.2	5164	98.2
7-15	160	73.0	26	15.4	5180	100.4
8-14	160	75.5	26	15.9	5229	101.4
9-13	170	90.5	28	18.6	5456	110.0
10-12	170	87.5	27	17.8	5394	106.7
11-11	170	90.0	27	18.7	5461	108.2
12-5	160	71.0	24	15.3	5169	96.3
13-6	190	109.5	31	21.9	5681	121.6
14-10	190	105.0	31	21.0	5623	120.0
15-9	210	122.5	38	24.5	5844	126.0
16-4	210	116.5	39	21.9	5684	136.4

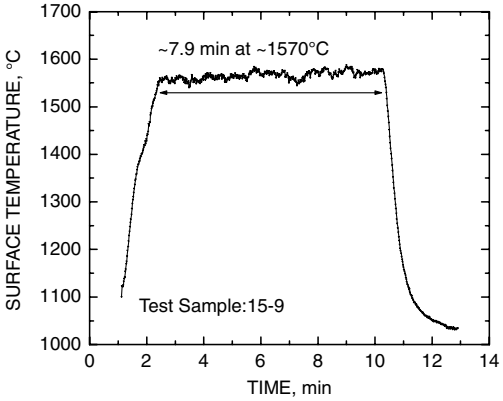

Fig. 3 Transient surface temperature profile for test 15 sample 9 run at 210 kW for a target test time of 10 min.

contribution to heating is required to account for the higher estimated hot-wall heat flux.

Figure 4 illustrates the uncertainty associated with the determination of catalytic efficiency, using case 10–12 as an example. The measured wall temperature (to four digits) is 1436°C, and the estimated hot-wall heat flux for $\varepsilon = 0.90$ is 43.5 $W \cdot cm^{-2}$; this location is shown by the solid symbol in the heat flux abacus of Fig. 4, giving a derived catalytic efficiency of 2.65×10^{-3}. Three sources contribute to the uncertainty of this value. First, the ± 10C° uncertainty in the wall temperature measurement is shown by the horizontal error bars. Second, the freestream enthalpy can be determined reasonably within a 10% accuracy [26], limited mainly by the uncertainty in the cold-wall heat flux measurement. The contribution of this uncertainty is indicated by the pair of symmetric vertical error bars closest to the solid symbol. Finally, the more widely spread asymmetric vertical error bars indicate the uncertainty introduced by the surface temperature and emittance together into the radiative heat flux computation. The emittance uncertainty is taken here as $+0.1/-0.2$, because emittance cannot exceed 1 by definition. The catalytic efficiency of 0.842×10^{-3} derived by assuming an emittance of 0.75 is also plotted in Fig. 4 as an open symbol and lies within this error bound. The emittance makes the dominant contribution to the radiative heat flux uncertainty and, thus, to the catalytic efficiency uncertainty. For this case, the uncertainty in γ' is seen to approach an order of magnitude.

Tables 3 and 4 show that atomic oxygen is the dominant oxygen species at the sample surface under all test conditions, with O_2 and NO number densities typically 1 or more orders of magnitude lower than O-atom number densities. The O-atom number densities computed for $\varepsilon = 0.90$ and 0.75 typically differ by less than 2%. Oxygen is essentially fully dissociated at all Plasmatron powers used in this study, but nitrogen dissociation is predicted to rise with increasing power. The N- and O-atom number densities at the sample surface become similar at the highest Plasmatron powers. Slightly larger N-atom concentrations near the surface are computed for $\varepsilon = 0.75$ than for 0.90.

Table 2 UHTC heating conditions

Test-Sample	Time[a], min	T_w, °C	q_w[b], $W \cdot cm^{-2}$ $\varepsilon = 0.75$	$\varepsilon = 0.90$
5-20	10 (8.2)	1240	22.4	26.8
6-16	10 (7.7)	1390	32.3	38.8
7-15	5 (3.2)	1360	30.0	35.9
8-14	20 (18.0)	1390	32.3	38.8
9-13	10 (8.3)	1460	38.2	45.8
10-12	20 (18.3)	1440	36.3	43.5
11-11	5(3.9)	1460	38.0	45.6
12-5	16 (14.0)	1350	29.7	35.6
13-6	20 (17.3)	1510	43.2	51.8
14-10	10 (8.3)	1500	42.3	50.8
15-9	10 (7.9)	1570	49.5	59.4
16-4	15 + 5	1550	46.7	56.0

[a]Target test time (approximate time at T_w).
[b]From $q_w = \varepsilon\sigma T_w^4 + q_{cond}$, with $q_{cond} = 0$.

B. Oxide Formation

All UHTC test specimens survived the Plasmatron exposures with minimal dimensional and mass changes and without any visual evidence of mechanical failure, such as chipping associated with spalling or specimen fractures induced by the thermal cycle between room temperature and the test temperature. This was true even during the initial exploratory tests that resulted in the failure of the SiC model cover.

Figure 5 shows measured changes in the total sample mass and thickness as a function of target test time and surface temperature. For fixed test times, the samples generally gained the most mass and thicknesses at the lower temperatures, with these gains decreasing or turning into net losses at the higher temperatures.

All posttest UHTC surfaces were black, shiny, and smooth on a macroscopic scale, indicative of the formation of a glassy oxide layer. Figure 6 shows SEM images of the oxidized surfaces (top row) and cross sections (bottom row) of samples 20, 16, and 9. These samples were exposed to the Plasmatron flow for target test times of 10 min at increasing power levels, attaining correspondingly higher surface temperatures. At this magnification, the surfaces are inhomogeneous, mostly covered by a glassy coating, but with regions of exposed crystalline material. Chemical analysis by EDS confirms the presence of Zr and O in the exposed crystallites and Si and O in the glassy phase, consistent with the anticipated oxidation products ZrO_2 and SiO_2. Boron was not detected by EDS, but may be present in small quantities because light elements are difficult to quantify by EDS.

The surface morphologies differ on the different samples. On sample 20, the glassy layer appears as a thin patchy film with many small, well-dispersed regions of exposed ZrO_2 grains. On sample 16, most of the surface is covered with a uniform glassy film, with only a few exposed regions. On sample 9, the glass film appears thicker and

Table 3 Catalytic efficiencies and species number densities at the surface for $\varepsilon = 0.75$

		Number Density, $\times 10^{23}$ m^{-3}				
Test-Sample	γ', $\times 10^{-3}$	$[N_2]$	[N]	[O]	$[O]/[O_2]$	[O]/[NO]
5-20	0.333	2.97	0.0444	1.75	122	460
6-16	1.04	2.44	0.379	1.53	178	675
7-15	0.285	2.37	0.516	1.56	653	1420
8-14	0.681	2.33	0.504	1.52	309	973
9-13	0.936	2.04	0.728	1.41	291	933
10-12	0.842	2.13	0.666	1.44	304	959
11-11	0.911	2.04	0.734	1.41	300	949
12-5	0.349	2.40	0.488	1.56	533	1300
13-6	0.680	1.70	1.05	1.31	498	1220
14-10	0.828	1.79	0.955	1.33	389	1090
15-9	1.13	1.52	1.16	1.23	334	988
16-4	1.15	1.69	1.01	1.28	298	935

Table 4 Catalytic efficiencies and species number densities at the surface for $\varepsilon = 0.90$

		Number Density, $\times 10^{23}$ m^{-3}				
Test-Sample	γ', $\times 10^{-3}$	$[N_2]$	[N]	[O]	[O]/[O_2]	[O]/[NO]
5-20	2.33	3.05	0.000203	1.49	7.47	34.4
6-16	2.91	2.66	0.157	1.50	42.9	202
7-15	1.78	2.57	0.301	1.55	94.1	405
8-14	2.36	2.55	0.279	1.51	69.7	314
9-13	2.81	2.30	0.483	1.43	80.1	354
10-12	2.65	2.35	0.426	1.44	79.2	352
11-11	2.78	2.27	0.486	1.41	81.8	361
12-5	1.87	2.61	0.270	1.56	84.7	371
13-6	2.56	1.93	0.793	1.32	118	485
14-10	2.73	2.02	0.702	1.34	103	436
15-9	3.27	1.77	0.888	1.25	101	428
16-4	3.19	1.92	0.753	1.29	93.3	402

more continuous than on sample 20, but with large regions of partially exposed ZrO_2 grains.

The cross-sectional SEM images of Fig. 6 reveal a partially oxidized sublayer extending below the outer glassy layer in all three specimens. Figure 7 shows a higher-magnification SEM image of the two-layer oxide structure formed on sample 9, along with XRD spectra (plotted as diffracted x-ray intensity versus twice the diffraction angle) collected in each layer. The diffraction pattern suggests that monoclinic zirconia (m-ZrO_2) is the major phase in the outer glassy layer (layer 1), but the amorphous glassy phases produce no diffraction peaks. The m-ZrO_2 peaks must originate from exposed crystalline regions in layer 1. The SEM image reveals some porosity

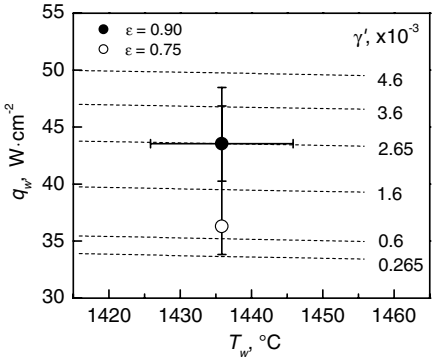

Fig. 4 Heat flux abacus for the determination of the catalytic efficiency for case 10-12 with uncertainty bars: temperature (horizontal), free stream enthalpy (symmetric, narrow vertical), and radiative flux (asymmetric, wide vertical).

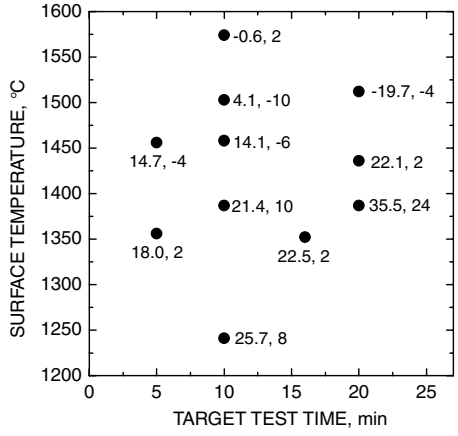

Fig. 5 Changes in total sample mass (in milligrams) and average sample thickness (in microns) as a function of surface temperature and target test time in the Plasmatron stream.

in the sublayer (layer 2), and the XRD spectrum indicates that m-ZrO_2, hexagonal α-SiC, and ZrB_2 are present.

The XRD spectrum of layer 1 shows an additional peak near 30 deg that was not detected in layer 2. This peak may indicate the presence of t-ZrO_2, the high-temperature tetragonal phase of zirconia quenched by rapid cooling, or a partially nitrided zirconia phase, such as $Zr_7O_{11}N_2$ [27]. Monteverde and Bellosi [6] cycled ZrB_2–SiC–Si_3N_4 composites in atmospheric-pressure air up to 1350°C and assigned a similar peak in their surface XRD spectra to t-ZrO_2, hypothesizing that this phase was stabilized by impurities.

The presence of a nitrided zirconia phase on the surface of sample 9 is plausible in view of the high N-atom concentration in the boundary layer during run 15; see Tables 3 and 4. The characteristic XRD peaks of $Zr_7O_{11}N_2$ fit very well with the unidentified peaks shown in the layer 1 spectrum. Quantitative calculations using the layer 1 XRD spectrum and the structural parameters of m-ZrO_2 and $Zr_7O_{11}N_2$ single crystals indicate that the mass fraction of $Zr_7O_{11}N_2$ is ~10%. The nitridation of ZrO_2 on the surface on the sample 9 surface was additionally investigated by XPS. Figure 8 shows the N 1s core level feature in the measured XPS spectrum near 398 eV, confirming the presence of nitrogen atoms in the oxidized surface.

Figures 9a and 9b show measurements of oxide layer thickness as a function of test temperature and time. Each point is the average of ~10 measurements made on high-magnification cross-sectional SEM images of regions with relatively uniform glassy surface oxide layers. The SEM images chosen for analysis, though necessarily selective, are representative of the oxide formed on each specimen. The error bars indicate scatter in the measurements for each analyzed image; larger variations in layer thicknesses are expected over the samples as a whole.

The figures demonstrate that the glassy outer layer thickens with increasing temperature (1250, 1390, 1570°C) for a fixed test time of 10 min and thickens with increasing test times (5, 10, 20 min) at a fixed surface temperature in the 1360–1390°C range. Both the surface and sublayers in Fig. 9b exhibit parabolic growth in time, consistent with diffusion-limited oxidation. Figure 9a shows that growth of the glassy outer layer accelerates with increasing temperature, but that the sublayer is thickest at low temperatures, has a minimum at intermediate temperatures, and increases again at high temperatures. This behavior must reflect a balance between temperature-dependent transport and reaction kinetics, which increase with temperature and favor oxidation, and the thickening outer glassy layer, which hinders oxygen diffusion and suppresses oxidation.

Figures 10a and 10b show surface SEM images of samples oxidized in a furnace for 20 min at 1250 and 1575°C, respectively, at a total air pressure of 10^4 Pa. The surface oxides formed on the ZrB_2–30SiC specimens in the furnace environment and the Plasmatron environment under similar temperature and total pressure conditions are very different. At 1250°C, glassy oxide and exposed zirconia grains on the furnace-oxidized sample are segregated into much larger regions than on the Plasmatron-oxidized sample. Note the factor of 5 difference in magnification between the

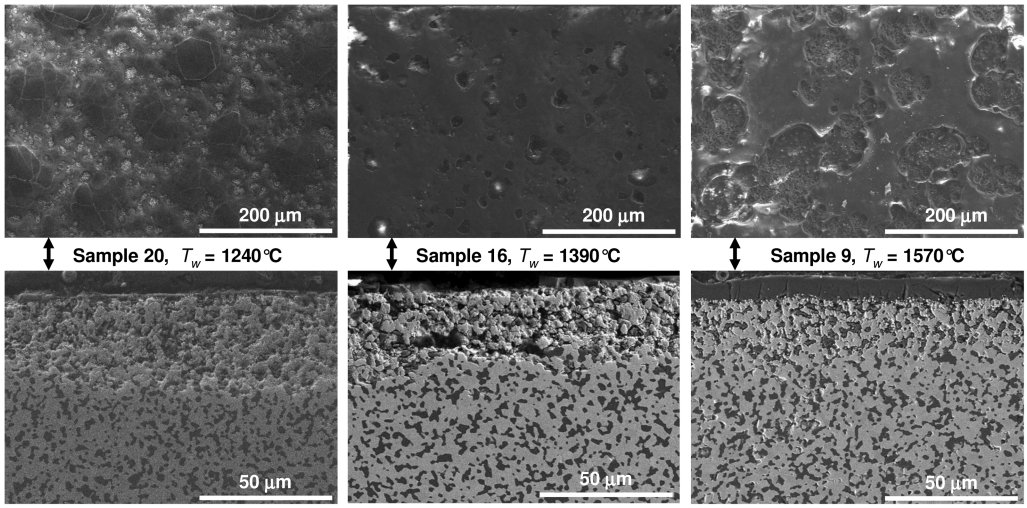

Fig. 6 Posttest SEM images of samples 20, 16, and 9, which reached quasi-steady surface temperatures of 1240, 1390, and 1570°C during exposure to the Plasmatron flow for 10 min at different power levels. The top row shows the oxidized surfaces, and the bottom row shows the cross sections showing oxidized layers.

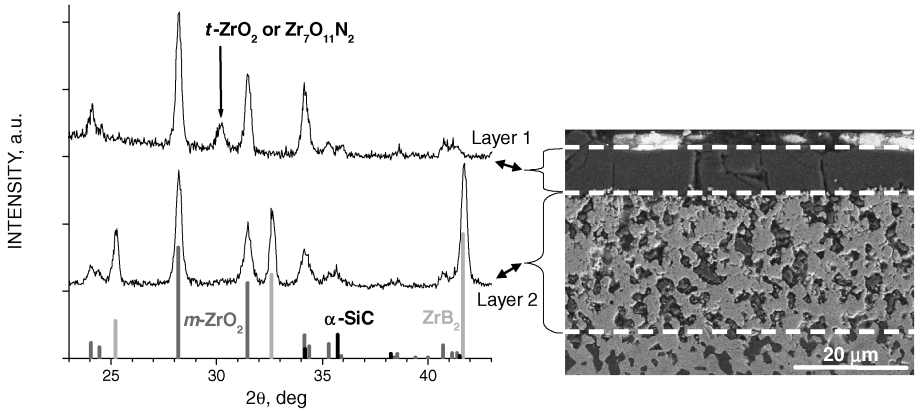

Fig. 7 XRD spectra of the oxidized layers on sample 9.

surface SEM images of Figs. 6 and 10. At the higher furnace temperature, the surface is made up of zirconia grains in a glassy matrix with no indication of a distinct overlaying glassy layer as observed for sample 9 oxidized in the Plasmatron. The furnace-oxidized sample at 1575°C appears white/gray in contrast to the black color of sample 9.

C. Optical Properties

Changes in the hemispherical-directional spectral reflectance measured before and after exposure to the plasma flow are shown in Fig. 11a for samples 5 and 6. Reflectance measurements performed on other pre- and posttest samples were very similar, with little discernible dependence on Plasmatron power or sample exposure time.

In all cases, exposure to the plasma stream leads to a significant drop in reflectance, with posttest values around 0.1 for most of the spectral range. ZrB_2 has metallic electrical properties, with a room-temperature electrical resistivity of about 8 $\mu\Omega$ cm [28]. In the infrared region, a large drop in reflectance is consistent with the

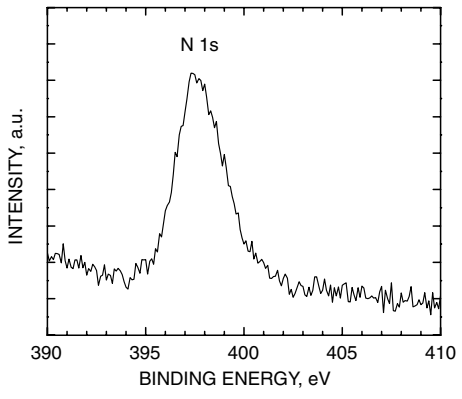

Fig. 8 The N 1s feature in the XPS spectrum of the surface layer of sample 9.

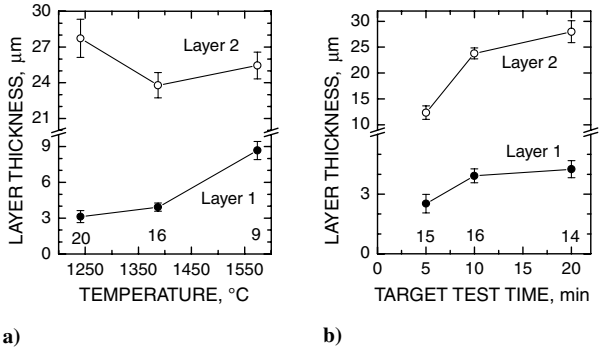

Fig. 9 Oxide layer thicknesses estimated from SEM images of samples exposed to the Plasmatron stream: a) samples 20, 16, and 9 oxidized for similar times (~10 min) at increasing temperatures, and b) samples 15, 16, and 14 oxidized at similar temperatures (1360–1390°C) for increasing test times.

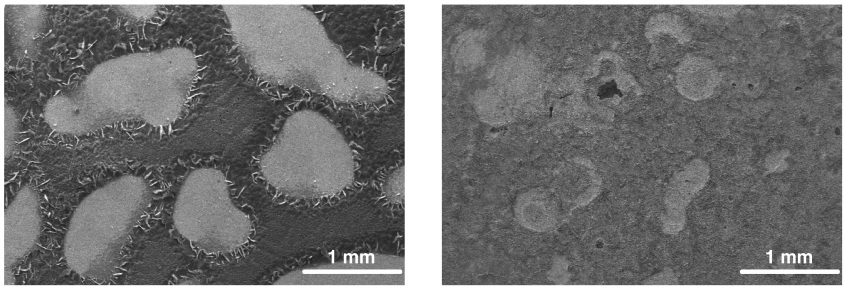

a) b)

Fig. 10 Surface SEM images of samples oxidized in a furnace in 10^4 Pa air for 20 min at two different temperatures: a) 1250°C, and b) 1575°C.

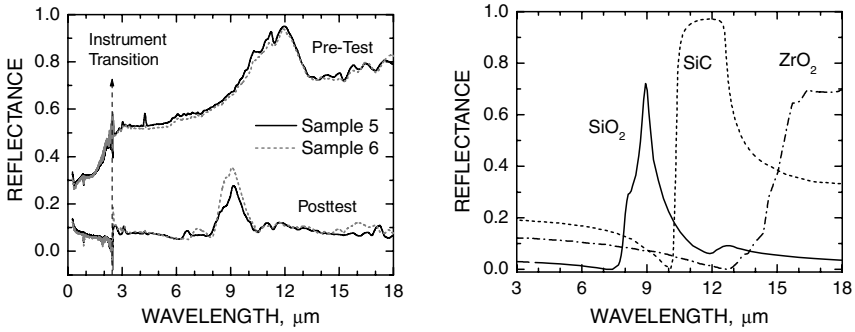

a) b)

Fig. 11 Comparison of measured and calculated reflectance spectra: a) experimental hemispherical-directional spectral reflectance of samples 5 and 6 before and after exposure to the plasma flow, and b) normal spectral reflectance computed for SiO_2, SiC, and ZrO_2 from published optical constants.

conversion of the UHTC surface layer from metallic to dielectric by oxidation of ZrB_2 and SiC. In the visible region, this drop in reflectance explains the color change in specimen surfaces from a metallic gray to a deep black after exposure to the plasma flow.

Some structure is evident in the measured spectra: a broad peak in the 10–13 μm range for the pretest samples and a sharper feature centered near 9 μm for the posttest samples. Figure 11b shows that similar features are found in theoretical reflectance spectra computed for a semi-infinite dielectric at normal incidence [29] using published optical constant data for SiC and SiO_2 [30]. These reflectance features derive from the stretching mode vibrations of Si–C and Si–O bonds in the virgin and oxidized UHTC composite, respectively. Figure 11b includes a similar calculation for ZrO_2 using the optical constants of Synowicki and Tiwald [31]. The predicted ZrO_2 reflectance feature above 14 μm is not observed in the experimental spectra. The presence of the SiO_2 feature and the absence of the ZrO_2 feature correlate reasonably well with the SEM microscopy of the posttest specimens that show a glassy outer layer with only minor amounts of exposed ZrO_2 on the surface.

Figures 12a and 12b show close-ups of the Si–O stretching mode reflectance feature for the same specimens in Figs. 9a and 9b, respectively. Growth of the reflectance feature in Fig. 12a correlates well with the significantly increasing glassy layer thickness with temperature in Fig. 9a (3.1–8.7 μm), whereas Fig. 12b shows the relative insensitivity of the feature to more moderate thickness changes with time in Fig. 9b (2.5–4.3 μm).

Temperature-dependent total hemispherical emittance values can be estimated from room-temperature spectral reflectance measurements by using optical relations for an opaque solid and Kirchhoff's law to convert spectral reflectance into spectral emittance and then averaging the spectral emittance weighted by the Planck function for different temperatures. This procedure presumes that weighting by the Planck function, rather than temperature-dependant optical constants, dominates the temperature-dependant total emittance. Figure 13 shows the results of such an estimate calculated from the spectral reflectance data of Fig. 11a. The predicted emittance of the oxidized specimens is quite high, near 0.9 over the entire temperature

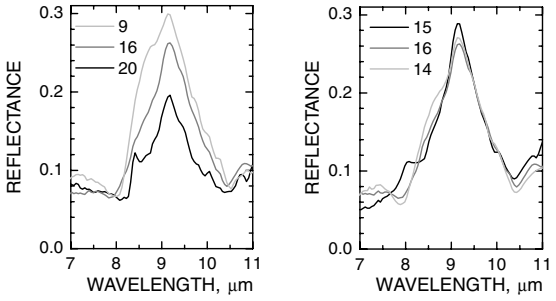

a) b)

Fig. 12 Si–O stretching mode reflectance feature: a) samples 20, 16, and 9 tested for 10 min at 1250, 1390, and 1570°C; and b) samples 15, 16, and 14 tested at 1360–1390°C for 5, 10, and 20 min.

range, whereas that of the virgin UHTC rises from a low value of ~0.25 at room temperature to ~0.6 at 2000°C. Because differences in the Plasmatron operating conditions had very little influence on reflectance spectra as a whole, the estimated emittances of all posttest

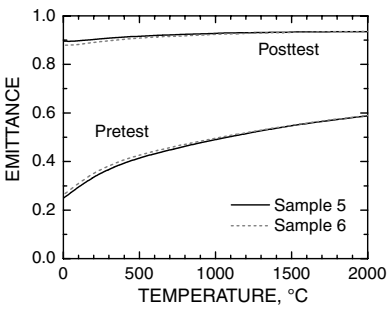

Fig. 13 Temperature-dependent total hemispherical emittance estimated from room-temperature spectral reflectance measurements.

samples are essentially identical to those shown for samples 5 and 6 in Fig. 13.

The emittance of a UHTC specimen will change as its surface progressively oxidizes during a Plasmatron test. The true instantaneous hemispherical emittance during a test run may lie between these pre- and posttest estimates, particularly during the initial heat-up of the specimen upon insertion. The lower value of $\varepsilon = 0.75$ used in our hot-wall heat flux estimates lies within these bounds and is in good agreement with the measurements of total hemispherical emittance performed at temperatures between 1000 and 1700°C on ZrB_2–15SiC–2$MoSi_2$ composites by Scatteia et al. [32] The higher value of $\varepsilon = 0.90$ is consistent with our posttest reflectance measurements and also with the results of Monteverde and Savino [33], who recently tested hot-pressed ZrB_2–15SiC in an 80 kW plasma torch and derived an in situ emittance of ~0.9 from simultaneous two- and one-color radiometry measurements.

D. Catalytic Properties

In Fig. 14, we compare catalytic efficiencies derived in the present work with laboratory measurements reported by Scatteia et al. [32] and Marschall et al. [34] for similar hot-pressed ZrB_2-based composites. Measurements by Scatteia et al. were performed in the MESOX facility, which uses a solar furnace to heat specimens to high temperatures, a microwave-discharge flow tube to generate partially dissociated air, and an optical emission spectroscopy combined with actinometry to measure O-atom density gradients near the sample surface. Measurements by Marschall et al. were performed in a diffusion-tube side-arm reactor using a microwave discharge to generate binary O/O_2 or N/N_2 mixtures and two-photon laser-induced fluorescence detection of O-atom or N-atom concentration gradients. Experimental facilities, measurement techniques, and data analysis methods have been described in detail in the literature, for both the MESOX [35–39] and the side-arm reactor [40–44] setups.

The MESOX and the side-arm reactor laboratory measurements derive values of the atom catalytic efficiency γ, whereas the experiments in the Plasmatron give values of the catalytic efficiency $\gamma' = \gamma\beta$. Marschall et al. performed measurements at relatively low temperatures (up to 650°C). Silicon carbide oxidation is negligible in this temperature range. The primary oxidation products are B_2O_3 and ZrO_2, and the surface catalytic efficiency decreased once the melting point of B_2O_3 (~450°C) was exceeded. All of the MESOX and Plasmatron data were obtained at temperatures well above 450°C.

Figure 14 shows that γ' values from Plasmatron experiments performed over a 1200–1700°C surface temperature range are factors of 5–20 times smaller (depending on the value of emittance used in the hot-wall heat flux estimate) than γ values from the MESOX experiments. In this temperature range, SiC oxidation becomes increasingly important and, in both experiments, the oxidized UHTC surfaces are covered with a glassy silica-based oxide layer. If the silica-based surfaces are assumed to be similar in the two experiments, Fig. 14 implies that the exothermic recombination energy is not fully accommodated to the surface, with β roughly in the 0.2–0.05 range. Rutigliano et al. [45] and Bedra et al. [46] have recently performed molecular dynamics simulations for N-atom recombination on β-crisobalite and O-atom recombination on quartz surfaces, respectively. In both studies, β was found to be about 0.4. Values of γ around 0.01 are generally consistent with measurements on silica surfaces at these temperatures [25].

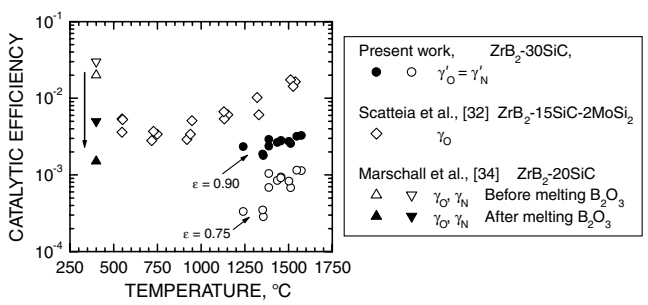

Fig. 14 Comparison of catalytic efficiencies determined for ZrB_2–SiC UHTC materials; measurements of Scatteia et al. [32] were performed in the MESOX facility and those of Marschall et al. [34] in a side-arm diffusion-tube reactor.

V. Discussion

The oxide morphologies of the UHTC samples exposed to the Plasmatron stream suggest the following explanations. At temperatures below ~1000°C, SiC oxidation is negligible and only the ZrB_2 component of the UHTC composite oxidizes significantly [12]. The lowest-power Plasmatron test produces a slightly higher surface temperature of 1240°C (sample 20), at which SiC oxidation becomes more important, but is still slow compared with ZrB_2 oxidation. This condition limits the formation of SiO_2 relative to ZrO_2 and B_2O_3. However, the vapor pressure of liquid B_2O_3 at this temperature is already high, and the evaporation of boron oxide is significant. As a result, the borosilicate glass formed is only semiprotective as an oxygen barrier, and in-depth oxidation of ZrB_2 and SiC proceeds readily, resulting in a relatively thick sublayer of partially oxidized UHTC material. At moderately higher surface temperatures, like the 1390°C experienced by sample 16, the oxidation rate of SiC becomes sufficiently high to form a continuous glassy layer over the oxidized UHTC surface, slowing in-depth oxidation by limiting inward oxygen diffusion. At the highest Plasmatron test temperature of 1570°C (sample 9), SiC oxidation is even more rapid and an even thicker silica-rich glassy layer develops. However, at this temperature the added protection provided by the thicker glassy layer is somewhat mitigated by faster oxygen diffusion rates in the glass, resulting in a partially oxidized sublayer thicker than sample 16, but still thinner than sample 20.

With rising temperature, the combination of decreasing glass viscosity and increasing in-depth SiC oxidation can lead to greater gas formation rates below the glassy layer and, potentially, bubble formation. This interpretation is consistent with the surface SEM images of Figs. 6; the larger areas of exposed zirconia grains on sample 9 have an appearance that suggests the bursting of bubbles formed by gases evolving from beneath a relatively thick glassy layer, whereas on sample 20 the exposed areas are more consistent with direct oxidation of ZrB_2 to ZrO_2 on the outer surface.

Comparison of furnace-oxidized specimens with Plasmatron-exposed specimens suggests that the formation of silica is faster and/or the volatilization of silica is slower in the dissociated oxygen environment of the Plasmatron as compared with the furnace environment. Simple Gibb's free energy calculations based on thermodynamic data from [47] show that the reaction of SiC with atomic oxygen has a larger thermodynamic driving force than the reaction with molecular oxygen. Similar thermodynamic computations show that the equilibrium partial pressure of SiO gas over SiO_2 is higher in an atmosphere of 2×10^3 Pa O_2 (furnace environment) than in an atmosphere of 3×10^3 Pa O atoms (Plasmatron environment) for all temperatures in our experiments.

Experiments at ~900°C using a microwave-discharge source to generate atomic oxygen in a ~400 Pa O_2/Ar mixture have shown dramatically increased silica formation on Si wafers, and SiC and Si_3N_3 thin films, over similar experiments without atomic oxygen [48]. The O-atom densities in these discharge experiments were 2–4 orders of magnitude lower than in the Plasmatron tests.

Balat et al. [49,50] have studied the active–passive oxidation transition boundary of silicon carbide in standard and microwave-excited air. The theoretical transition temperature between active and passive SiC oxidation, computed using Wagner's model for boundary-layer diffusion-limited surface oxidation [51], was determined to be the same for molecular and atomic oxygen when the latter was expressed as equivalent molecular oxygen partial pressure (i.e., $P_{O_2} = 0.5P_O$) [50]. Experimentally, however, they found that the temperature–pressure domain characterized by passive silica formation on sintered SiC specimens was significantly

enlarged over the theoretical domain by oxygen dissociation [49,50]. Both our highest-temperature furnace oxidation (at 1575°C) and the two highest-power Plasmatron tests (15-9 and 16-4) lie just inside the active SiC oxidation regime as calculated by Balat et al. [49,50]. Our finding of a glassy outer layer on sample 9 (Fig. 6) versus a largely zirconia surface on the 1575°C furnace-tested specimen (Fig. 10) is consistent with the hypothesis of an expanded passive oxidation domain under dissociated oxygen.

In general, surface properties like emittance and catalytic efficiency depend on both the chemical nature and the microstructure of the surface. Based on spectral reflectance measurements, and the temperature-dependent total emittance behavior estimated from these data, oxidation in the Plasmatron increases the emittance of the ZrB_2–30SiC materials. This result is in good agreement with the measurements of Scatteia et al. [32], who showed that the emittance of ZrB_2–15SiC–2$MoSi_2$ composites heated in an oxidizing environment was always higher than that of specimens heated under vacuum. Despite differences in the morphology of the posttest surfaces (e.g., Fig. 6), reflectance spectra varied little over most of the spectral range (except in the immediate vicinity of the Si–O stretching mode feature between 7 and 11 μm), leading to an essentially identical estimated temperature-dependant total emittance behavior for all posttest specimens. In a very recent study, Scatteia et al. [52] investigated the effects of diamond tool versus electrical discharge machining methods (producing different surface roughness) on the emittance of ZrB_2–15SiC and ZrB_2–10HfB_2–15SiC materials. They found little difference between the samples once the surfaces were oxidized, concluding that the chemical composition of the oxide was the dominant factor over surface morphology in determining emittance.

Ito et al. [53] tested ZrB_2-based UHTC specimens in a flat-face stagnation point configuration similar to ours (see Fig. 1b) in a 110 kW ICP wind tunnel at gas enthalpies of 16–21 $kJ \cdot g^{-1}$, reaching surface temperatures of between about 1400 and 1850°C. The samples became whitish after testing at their highest heating conditions. Ito et al. interpreted an apparent jump in sample surface temperature with increasing gas enthalpy (near 19 $kJ \cdot g^{-1}$) as a reflection of decreasing emittance and increasing catalytic efficiency due to sample oxidation. No sample manufacturing information or posttest characterization results were presented, though the whitish surface is identified by the authors as "oxidized zirconium," suggesting that no silica former was incorporated. By contrast, the formation of a borosilicate glassy layer on the ZrB_2–30SiC specimens tested at VKI resulted in a black posttest surface with relatively high emittance and moderate catalytic efficiency, as reflected by the lower steady-state surface temperatures for higher stream enthalpies.

Monteverde and Savino [33] have recently tested a hot-pressed ZrB_2–15SiC composite at atmospheric pressure in an 80 kW plasma torch facility located at the University of Naples. Samples were diamond machined into hemispherical test specimens with a 7.5 mm radius. Tests were run at total enthalpies between 14 and 20 $kJ \cdot g^{-1}$, reaching surface temperatures of up to 1930°C for up to 4.5 min. Posttest sample surfaces were smooth and dark in appearance. Sample emittance during testing, derived by simultaneous two- and one-color radiometry measurements, was about 0.9. Simulations of fully catalytic versus noncatalytic heating of the test specimens suggest that the oxidized UHTC surfaces must possess very low catalytic efficiency to explain the measured surface temperature transients. Both the optical and catalytic behaviors reported by Monteverde and Savino are generally consistent with those found in the present study. However, cross-sectional SEM images of their oxidized specimens reveal a somewhat different oxide structure, with the outer glassy layer and the virgin UHTC material separated by a distinct layer of ZrO_2 imbedded in glass over a thinner SiC-depleted layer. Similar multilayer oxide structures have been reported in furnace experiments and arcjet tests [14]. In the present study, only a single sublayer of partially oxidized UHTC is observed, perhaps because the temperatures were not sufficiently high and/or the exposure times were not sufficiently long to fully deplete the SiC from the layer beneath the outer glassy scale. In furnace oxidation tests, SiC depletion is only significant at test temperatures approaching 1500°C, but it occurs readily at higher temperatures [12]. The depletion of SiC from the layer beneath the outer glassy layer occurs by active oxidation of SiC to SiO and CO, which has a strong temperature dependence [15].

VI. Conclusions

Ultrahigh-temperature ceramics are candidates for leading-edge and control surface applications on future hypersonic aerospace vehicles, for which sustained operation at surface temperatures of 1500–2000°C and above are desired [1,2]. In such flight environments, materials will be exposed to highly dissociated air, particularly atomic oxygen. This study tested materials in a partially dissociated air environment at the lower end of the desired temperature range, but with generally favorable results. Under the conditions of this study, exposure to cold-wall heat fluxes ranging from 51.0 to 122.5 $W \cdot cm^{-2}$ resulted in surface temperatures ranging from 1240 to 1570°C. The Plasmatron stream consisted of highly dissociated oxygen and, as heat flux increased, an increasing proportion of dissociated nitrogen. The exposures resulted in oxidation of the specimen surfaces, which produced an outer layer of silica-based glass and an underlying layer of ZrO_2 with some residual ZrB_2 and SiC. Changes in specimen dimensions and mass were minimal. The derived catalytic efficiency of the oxidizing surface was low ($\sim 10^{-3}$) and the measured posttest emittance was high ($\sim$0.9), both favorable properties that help lower the quasi-steady surface temperatures attained during hypersonic flight.

Future experiments are planned using a redesigned model configuration, which will enable higher-enthalpy/higher-temperature studies. In addition, other variables, such as the volume fraction of SiC in the UHTC composite and the composition of the UHTC material (HfB_2 vs ZrB_2), will be evaluated to determine their effects on the properties of the resulting surfaces. Additional diagnostics are planned for these experiments, in particular a wideband radiometer to enable in situ determination of the surface emittance and emission spectroscopic diagnostics for the detection of volatile species. The importance of the former diagnostic is evident, given the significant uncertainty that emittance introduces into evaluations of the surface test environment and such properties as catalytic efficiency. The value of the latter diagnostic was recently demonstrated in an adjunct to this test series in which the temporal emission signatures of volatile boron species were detected during UHTC oxidation in the Plasmatron; these results will be reported in a separate paper [54].

Acknowledgments

This research was supported by the Ceramics and Nonmetallic Materials Program of the U.S. Air Force Office of Scientific Research through contracts F49550-05-C-0020 (Marschall and Pejaković) and FA9550-06-0125 (Fahrenholtz and Hilmas), the National Science Foundation through grants DMR-0435856 (Marschall) and DMR-0346800 (Fahrenholtz and Zhu), and the European Office of Aerospace Research and Development through contract FA8655-06-1-3078 (Fletcher, Asma, and Thömel). The authors would like to thank Olivier Chazot at VKI for advice and support during Plasmatron testing, Eric Bohannan at the Missouri University of Science and Technology for XRD analysis, and Jeffry Wight at the Missouri University of Science and Technology for XPS analysis.

References

[1] Fuller, J., and Sacks, M., "Special Section: Ultra-High Temperature Ceramics," *Journal of Materials Science*, Vol. 39, No. 19, 2004, pp. 5885–6066. doi:10.1023/B:JMSC.0000041685.85043.34

[2] Fuller, J., Blum, Y., and Marschall, J., "Topical Issue on Ultra-High-Temperature Ceramics," *Journal of the American Ceramic Society*, Vol. 91, No. 5, 2008, pp. 1397–1502. doi:10.1111/j.1551-2916.2008.02481.x

[3] Kuriakose, A. K., and Margrave, J. L., "The Oxidation Kinetics of Zirconium Diboride and Zirconium Carbide at High Temperatures,"

Journal of the Electrochemical Society, Vol. 111, No. 7, 1964, pp. 827–831.
doi:10.1149/1.2426263

[4] Tripp, W. C., Davis, H. H., and Graham, H. C., "Effect of an SiC Addition on the Oxidation of ZrB_2," *Ceramic Bulletin*, Vol. 52, No. 8, 1973, pp. 612–616.

[5] Opeka, M. M., Talmy, I. G., Wuchina, E. J., Zaykoski, J. A., and Causey, S. J., "Mechanical, Thermal, and Oxidation Properties of Refractory Hafnium and Zirconium Compounds," *Journal of the European Ceramic Society*, Vol. 19, 1999, pp. 2405–2414.
doi:10.1016/S0955-2219(99)00129-6

[6] Monteverde, F., and Bellosi, A., "Oxidation of ZrB_2-Based Ceramics in Dry Air," *Journal of the Electrochemical Society*, Vol. 150, No. 11, 2003, pp. B552–B559.
doi:10.1149/1.1618226

[7] Monteverde, F., Bellosi, A., and Guicciardi, S., "Processing and Properties of Zirconium Diboride-Based Composites," *Journal of the European Ceramic Society*, Vol. 22, 2002, pp. 279–288.
doi:10.1016/S0955-2219(01)00284-9

[8] Sciti, D., Brach, M., and Bellosi, A., "Long-Term Oxidation Behavior and Mechanical Strength Degradation of a Pressurelessly Sintered ZrB_2–$MoSi_2$ Ceramic," *Scripta Materialia*, Vol. 53, 2005, pp. 1297–1302.
doi:10.1016/j.scriptamat.2005.07.026

[9] Sciti, D., Brach, M., and Bellosi, A., "Oxidation Behavior of a Pressureless Sintered ZrB_2–$MoSi_2$ Ceramic Composite," *Journal of Materials Research*, Vol. 20, No. 4, 2005, pp. 922–930.
doi:10.1557/JMR.2005.0111

[10] Opila, E., Levine, S., and Lorincz, J., "Oxidation of ZrB_2- and HfB_2-Based Ultra-High Temperature Ceramics: Effect of Ta Additions," *Journal of Materials Science*, Vol. 39, 2004, pp. 5969–5977.
doi:10.1023/B:JMSC.0000041693.32531.d1

[11] Levine, S. R., Opila, E. J., Halbig, M. C., Kiser, J. D., Singh, M., and Salem, J. A., "Evaluation of Ultra-High Temperature Ceramics for Aeropropulsion Use," *Journal of the European Ceramic Society*, Vol. 22, 2002, pp. 2757–2767.
doi:10.1016/S0955-2219(02)00140-1

[12] Rezaie, A., Fahrenholtz, W. G., and Hilmas, G. E., "Evolution of Structure During the Oxidation of Zirconium Diboride-Silicon Carbide in Air up to 1500°C," *Journal of the European Ceramic Society*, Vol. 27, 2007, pp. 2495–2501.
doi:10.1016/j.jeurceramsoc.2006.10.012

[13] Rezaie, A., Fahrenholtz, W. G., and Hilmas, G. E., "Oxidation of Zirconium Diboride-Silicon Carbide at 1500°C at a Low Partial Pressure of Oxygen," *Journal of the American Ceramic Society*, Vol. 89, No. 10, 2006, pp. 3240–3245.
doi:10.1111/j.1551-2916.2006.01229.x

[14] Fahrenholtz, W. G., Hilmas, G. E., Talmy, I. G., and Zaykoski, J. A., "Refractory Diborides of Zirconium and Hafnium," *Journal of the American Ceramic Society*, Vol. 90, No. 5, 2007, pp. 1347–1364.
doi:10.1111/j.1551-2916.2007.01583.x

[15] Fahrenholtz, W. G., "Thermodynamic Analysis of ZrB_2–SiC Oxidation: Formation of a SiC-Depleted Region," *Journal of the American Ceramic Society*, Vol. 90, No. 1, 2007, pp. 143–148.
doi:10.1111/j.1551-2916.2006.01329.x

[16] Chamberlain, A. L., Fahrenholtz, W. G., and Hilmas, G. E., and Ellerby D. T., "High-Strength Zirconium Diboride-Based Ceramics," *Journal of the American Ceramic Society*, Vol. 87, No. 6, 2004, pp. 1170–1172.

[17] Bottin, B., Carbonaro, M., Zemsch, S., and Degrez, G., "Aerothermodynamic Design of an Inductively Coupled Plasma Wind Tunnel," AIAA Paper 1997-2498, June 1997.

[18] Bottin, B., Paris, S., Van Der Haegen, V., and Carbonaro, M., "Experimental and Computational Determination of the VKI Plasmatron Operating Envelope," AIAA Paper 1999-3607, June 1999.

[19] Barbante, P. F., and Chazot, O., "Flight Extrapolation of Plasma Wind Tunnel Stagnation Region Flowfield," *Journal of Thermophysics and Heat Transfer*, Vol. 20, No. 3, 2006, pp. 493–499.
doi:10.2514/1.17185

[20] Barbante, P. F., Degrez, G., and Sarma, G. S. R., "Computation of Nonequilibrium High-Temperature Axisymmetric Boundary-Layer Flows," *Journal of Thermophysics and Heat Transfer*, Vol. 16, No. 4, 2002, pp. 490–497.
doi:10.2514/2.6723

[21] Magin, T., Vanden Abeele, D. P., and Degrez, G., "An Implicit Multiblock Solver for Inductive Plasma Flows," AIAA Paper 2000-2480, June 2000.

[22] Vanden Abeele, D. P., and Degrez, G., "Numerical Model of High-Pressure Air Inductive Plasma Under Thermal and Chemical Non-Equilibrium," AIAA Paper 2000-2416, June 2000.

[23] Bottin, B., Vanden Abeele, D. P., Carbonaro, M., Degrez, G., and Sarma, G. S. R., "Thermodynamic and Transport Properties for Inductive Plasma Modeling," *Journal of Thermophysics and Heat Transfer*, Vol. 13, No. 3, 1999, pp. 343–350.
doi:10.2514/2.6444

[24] Garcia, A.Chazot, O., and Fletcher, D. G., "Investigations in Plasmatron Facilities on Catalycity Determination," *Proceedings of the 4th European Symposium on Aerothermodynamics for Space Vehicles*, SP-487, ESA, Paris, 2002, pp. 489–495.

[25] Bedra, L., and Balat-Pichelin, M., "Comparative Modeling Study and Experimental Results of Atomic Oxygen Recombination on Silica-Based Surfaces at High-Temperature," *Aerospace Science and Technology*, Vol. 9, 2005, pp. 318–328.
doi:10.1016/j.ast.2005.01.011

[26] Thömel, J., Rini, P., and Chazot, O., "Sensitivity Analysis of the Local Heat Transfer Simulation for the Application to Thermal Protection Systems," AIAA Paper 2006-3813, June 2006.

[27] Lerch, M., "Nitridation of Zirconia," *Journal of the American Ceramic Society*, Vol. 79, No. 10, 1996, pp. 2641–2644.

[28] Rahman, M., Wang, C. C., Chen, W., and Akbar, S. A., "Electrical Resistivity of Titanium Diboride and Zirconium Diboride," *Journal of the American Ceramic Society*, Vol. 78, 1995, pp. 1380–1382.
doi:10.1111/j.1151-2916.1995.tb08498.x

[29] Heavens, O. S., *Optical Properties of Thin Solid Films*, Dover, New York, 1965.

[30] Palik, E. D. (ed.), *Handbook of Optical Constants of Solids; Vol. I*, Academic Press, New York, 1985.

[31] Synowicki, R. A., and Tiwald, T. E., "Optical Properties of Bulk c-ZrO_2, c-MgO, and a-As_3S_3 Determined by Variable Angle Spectroscopic Ellipsometry," *Thin Solid Films*, Vols. 455–456, 2004, pp. 248–255.
doi:10.1016/j.tsf.2004.02.028

[32] Scatteia, L., Borrelli, R., Cosentino, G., Bêche, E., Sans, J.-L., and Balat-Pichelin, M., "Catalytic and Radiative Behaviors of ZrB_2–SiC Ultrahigh Temperature Ceramic Composites," *Journal of Spacecraft and Rockets*, Vol. 43, No. 5, 2006, pp. 1004–1012.
doi:10.2514/1.21156

[33] Monteverde, F., and Savino, R., "Stability of Ultra-High Temperature ZrB_2–SiC Ceramics Under Simulated Atmospheric Re-Entry Conditions," *Journal of the European Ceramic Society*, Vol. 27, 2007, pp. 4797–4805.
doi:10.1016/j.jeurceramsoc.2007.02.201

[34] Marschall, J., Chamberlain, A., Crunkleton, D., and Rogers, B., "Catalytic Atom Recombination on ZrB_2/SiC and HfB_2/SiC Ultrahigh-Temperature Ceramic Composites," *Journal of Spacecraft and Rockets*, Vol. 41, No. 4, 2004, pp. 576–581.
doi:10.2514/1.2879

[35] Balat, M., Czerniak, M., and Badie, J. M., "Thermal and Chemical Approaches for Oxygen Catalytic Recombination Evaluation on Ceramic Materials at High Temperature," *Applied Surface Science*, Vol. 120, 1997, pp. 225–238.
doi:10.1016/S0169-4332(97)00238-9

[36] Balat, M. J. H., Czerniak, M., and Badie, J. M., "Ceramic Catalysis Evaluation at High Temperature Using Thermal and Chemical Approaches," *Journal of Spacecraft and Rockets*, Vol. 36, No. 2, 1999, pp. 273–279.
doi:10.2514/2.3442

[37] Balat-Pichelin, M., "Oxidation and Catalycity of Thermal Protection Materials at High Temperature," *High Temperature Material Processes*, Vol. 8, No. 1, 2004, pp. 161–171.
doi:10.1615/HighTempMatProc.v8.i1.100

[38] Balat-Pichelin, M., Badie, J. M., Berjoan, R., and Boubert, P., "Recombination Coefficient of Atomic Oxygen on Ceramic Materials Under Earth Re-Entry Conditions by Optical Emission Spectroscopy," *Chemical Physics*, Vol. 291, 2003, pp. 181–194.
doi:10.1016/S0301-0104(03)00152-6

[39] Balat-Pichelin, M., and Vessel, A., "Neutral Oxygen Atom Density in the MESOX Air Plasma Solar Furnace Facility," *Chemical Physics*, Vol. 327, 2006, pp. 112–118.
doi:10.1016/j.chemphys.2006.03.034

[40] Marschall, J., "Experimental Determination of Oxygen and Nitrogen Recombination Coefficients at Elevated Temperature Using Laser-Induced Fluorescence," AIAA Paper 97-3879, Aug. 1997.

[41] Marschall, J., "Laboratory Determination of Thermal Protection System Materials Surface Catalytic Properties," *Experiment, Modeling and Simulation of Gas-Surface Interactions for Reactive Flows in Hypersonic Flights*, Educational Notes RTO-EN-AVT-142, RTO/NATO, Neuilly-sur-Seine, France, July 2007, pp. 11-1–11-32.

[42] Marschall, J., Copeland, R. A., Hwang, H. H., and Wright, M. J., "Surface Catalysis Experiments on Metal Surfaces in Oxygen and Carbon Monoxide Mixtures," AIAA Paper 2006-181, Jan. 2006.

[43] Pallix, J. B., and Copeland, R. A., "Measurement of Catalytic Recombination Coefficients on Quartz Using Laser-Induced Fluorescence," *Journal of Thermophysics and Heat Transfer*, Vol. 10, No. 2, 1996, pp. 224–233. doi:10.2514/3.779

[44] Sepka, S., Chen, Y.-K., Marschall, J., and Copeland, R. A., "Experimental Investigation of Surface Reactions in Carbon Monoxide and Oxygen Mixtures," *Journal of Thermophysics and Heat Transfer*, Vol. 14, No. 1, 2000, pp. 45–52. doi:10.2514/2.6488

[45] Rutigliano, M., Pieretti, A., Cacciatore, M., Sanna, N., and Barone, V., "N Atoms Recombination on a Silica Surface: A Global Theoretical Approach," *Surface Science*, Vol. 600, 2006, pp. 4239–4246. doi:10.1016/j.susc.2005.12.080

[46] Bedra, L., Rutigliano, M., Balat-Pichelin, M., and Cacciatore, M., "Atomic Oxygen Recombination on Quartz at High Temperature: Experiments and Molecular Dynamics Simulation," *Langmuir*, Vol. 22, No. 17, 2006, pp. 7208–7216. doi:10.1021/la0600321

[47] Chase, M. W., Jr., *NIST-JANAF Thermochemical Tables*, 4th ed., American Institute of Physics, New York, 1998.

[48] Rogers, B. R., Song, Z., Marschall, J., Queraltó, N., and Zorman, C. A., "The Effect of Dissociated Oxygen on the Oxidation of Si, Polycrystalline SiC and LPCVD Si_3N_4," *High Temperature Corrosion and Materials Chemistry V; Vol. PV 2004-16*, edited by E. Opila, The Electrochemical Society, Pennington, 2004, pp. 268–278.

[49] Balat, M. J. H., "Determination of the Active-to-Passive Transition in the Oxidation of Silicon Carbide in Standard and Microwave-Excited Air," *Journal of the European Ceramic Society*, Vol. 16, 1996, pp. 55–62. doi:10.1016/0955-2219(95)00104-2

[50] Balat, M., Flamant, G., Male, G., and Pichelin, G., "Active to Passive Transition in the Oxidation of Silicon Carbide at High Temperature and Low Pressure in Molecular and Atomic Oxygen," *Journal of Materials Science*, Vol. 27, 1992, pp. 697–703. doi:10.1007/BF02403882

[51] Wagner, C., "Passivity During the Oxidation of Silicon at Elevated Temperatures," *Journal of Applied Physics*, Vol. 29, 1958, pp. 1295–1297. doi:10.1063/1.1723429

[52] Scatteia, L., Alfano, D., Monteverde, F., Sans, J.-L., and Balat-Pichelin, M., "Effect of Machining Method on the Catalytic and Emissivity of ZrB_2 and ZrB_2–HfB_2-Based Ceramics," *Journal of the American Ceramic Society*, Vol. 91, No. 5, May 2008, pp. 1461–1468. doi:10.1111/j.1551-2916.2008.02325.x

[53] Ito, T., Kurotaki, T., Sumi, T., Fujita, K., Ishida, K., and Mizuno, M., "Evaluation of Surface Catalytic Effect on TPS in 110 kW ICP-Heated Wind Tunnel," AIAA Paper 2005-189, Jan. 2005.

[54] Playez, M., Fletcher, D. G., Marschall, J., Fahrenholtz, W. G., Hilmas, G. E., and Zhu, S., "Optical Emission Spectroscopy during Plasmatron Testing of ZrB_2–SiC Ultra-High Temperature Ceramic Composites," *Journal of Thermophysics and Heat Transfer*, Vol. 23, No. 2, 2009, pp. 279–285.